

Computational modelling and data-driven homogenisation of knitted membranes

Sumudu Herath^{1,3*}, Xiao Xiao^{2,3} and Fehmi Cirak³

¹*Department of Civil Engineering, University of Moratuwa, Moratuwa, Sri Lanka*

²*Inria, 2004 route des Lucioles, 06902 Sophia Antipolis, France*

³*Department of Engineering, University of Cambridge, Trumpington Street, Cambridge CB2 1PZ, U.K.*

SUMMARY

Knitting is an effective technique for producing complex three-dimensional surfaces owing to the inherent flexibility of interlooped yarns and recent advances in manufacturing providing better control of local stitch patterns. Fully yarn-level modelling of large-scale knitted membranes is not feasible. Therefore, we consider a two-scale homogenisation approach and model the membrane as a Kirchhoff-Love shell on the macroscale and as Euler-Bernoulli rods on the microscale. The governing equations for both the shell and the rod are discretised with cubic B-spline basis functions. The solution of the nonlinear microscale problem requires a significant amount of time due to the large deformations and the enforcement of contact constraints, rendering conventional online computational homogenisation approaches infeasible. To sidestep this problem, we use a pre-trained statistical Gaussian Process Regression (GPR) model to map the macroscale deformations to macroscale stresses. During the offline learning phase, the GPR model is trained by solving the microscale problem for a sufficiently rich set of deformation states obtained by either uniform or Sobol sampling. The trained GPR model encodes the nonlinearities and anisotropies present in the microscale and serves as a material model for the macroscale Kirchhoff-Love shell. After verifying and validating the different components of the proposed approach, we introduce several examples involving membranes subjected to tension and shear to demonstrate its versatility and good performance.

Received . . .

KEY WORDS: knitting; membranes; rods; finite deformations; homogenisation; data-driven; Gaussian processes

1. INTRODUCTION

Knitting is one of the most efficient and widely used techniques for producing fabric membranes. The recent advances in computational knitting make it possible to produce large complex three-dimensional surfaces in one piece without seams [1, 2]. On a modern programmable flat-bed knitting machine it is possible to produce even non-developable surfaces by a local variation of the stitch pattern consisting of an interlooped yarn. Most promisingly, the yarn can be replaced or integrated with electroactive or conductive yarns to produce novel interactive textiles with sensing and/or actuation capabilities [3, 4, 5]. Knitted membranes are usually very flexible because the primary deformation mechanism for the yarn is bending rather than axial stretching. Their unique stretchability and drapability properties make knitted membranes appealing as a reinforcement in composite components [6, 7]. If needed,

*Correspondence to: sumuduh@uom.lk

the stiffness can be increased by inserting straight high-strength fibres during the knitting process. Such reinforced membranes have been recently used as a formwork in architectural engineering [8]. Considering the recent advances in knitting, there is a need for efficient computational approaches for the analysis of large-scale knitted membranes.

For large-scale analysis of knitted membranes, the computational homogenisation approaches which take into account the deformation of the interlooped yarn on the microscale are crucial. There is an extensive amount of literature on finite element-based computational homogenisation of heterogeneous solids, see e.g. the reviews [9, 10, 11]. Two-scale homogenisation often referred to as FE^2 , combined with a yarn-level and a membrane-level finite element model has been also applied to woven and knitted fabrics [12, 13, 14, 15]. The boundary conditions of the microscale representative volume element (RVE) are given by the membrane deformation and in turn the averaged yarn stress in the RVE yields the membrane stress. However, such schemes are inefficient for knitted membranes with large deformations because of the need to solve a nonlinear problem at each quadrature point of the membrane. It is increasingly apparent that for nonlinear problems two-scale homogenisation must be considered in combination with a data-driven machine learning model [16]. The model can be trained in an off-line learning phase by solving the microscale problem for a sufficiently rich set of deformation states. Subsequently, the trained model provides a closed-form constitutive equation that is used in the macroscale model. As a machine learning model, for instance, neural networks or GPR models have been used [16, 17, 18, 19]. Alternatively, it is possible to formulate the macroscale finite element problem directly on the training data set bypassing the need to train a machine learning model [20, 21]. GPR regression is a well-studied Bayesian statistical method and provides as such a principled approach to dealing with epistemic and aleatoric uncertainties and issues such as overfitting [22]. Therefore, we approximate the response of the microscale yarn model with GPR. Their limitation to relatively small dimensions and number of training points is not relevant for this paper.

Owing to the relative slenderness of the yarn on the microscale and the membrane on the macroscale, they are best modelled as a rod and a shell, respectively. Evidently, this leads in comparison to a 3D solid model to an immense reduction in the number of degrees of freedom. The geometrically exact rod theories pioneered by Simo et al. [23, 24] provide a consistent and efficient framework for modelling rods undergoing finite deformations. Later contributions to geometrically exact rod theories include [25, 26, 27]. While in most of these classical rod models the transverse shear deformations are taken into account, in more recent Euler-Bernoulli type models they are neglected [28, 29]. The omission of the transverse shear effectively sidesteps the shear locking problem which is a major impediment in the analysis of slender rods. These new models are usually discretised using smooth B-spline basis functions due to the presence of the higher-order displacement derivatives in the energy functional. The Euler-Bernoulli type rod model introduced in this paper takes into account the stretching, bending and torsion of the yarn as well as the non-frictional rod-to-rod contact between yarns. Similar to the yarn, the fabric membrane can be modelled with geometrically exact shell theories going back again to Simo et al. [30, 31]. As for rods, in more recent Kirchhoff-Love type shell models the transverse shear deformations are neglected and the weak form is discretised using smooth B-splines or subdivision basis functions [32, 33, 34]. Although the bending resistance of knitted membranes is usually very small, a suitably chosen shell bending energy term can serve as a regularisation for wrinkling under compressive stresses [33, 35]. In this paper we make use of the Kirchhoff-Love subdivision shell implementation introduced in [36, 37].

The outline of the paper is as follows. In Section 2 we introduce our finite deformation rod model, its discretisation with B-splines as well as the treatment of rod-to-rod contact. Subsequently, in Section 3 we discuss the proposed microscale yarn-level RVE model for computational homogenisation. This model is verified and validated with experimental and numerical results from literature. In Section 4, we introduce the data-driven GPR model and describe its training with the yarn-level RVE model. Finally, in Section 5, we first discuss the

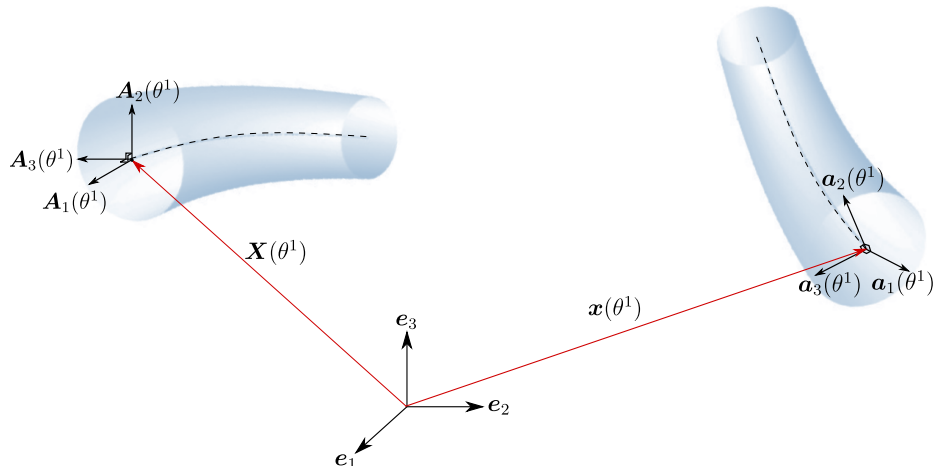


Figure 1. Geometric description of a spatial rod in its reference (left) and deformed (right) configurations. The two configurations are defined using the line of centroids $\mathbf{X}(\theta^1)$ and $\mathbf{x}(\theta^1)$ and the respective covariant basis vectors.

training of the GPR model and then analyse membranes subjected to tension to assess the accuracy of the obtained data-driven constitutive model.

2. FINITE DEFORMATION ANALYSIS OF YARNS

In this section we summarise the governing equations for the finite deformation Euler-Bernoulli rod model for the yarn. The presented equations are without loss of generality restricted to rods with circular cross-sections. We take into account rod-to-rod contact by enforcing the non-penetration constraint with the Lagrange multiplier method.

2.1. Kinematics

The geometry of the rod is described by a set of circular cross-sections connected by their line of centroids. In accordance with the Euler-Bernoulli assumption, equivalent to the Kirchhoff-Love assumption for shells and plates, transverse shear is neglected so that cross-sections remain always normal to the line of centroids.

The position vectors of material points in the reference and deformed configurations $\mathbf{R}(\theta^1, \theta^2, \theta^3)$ and $\mathbf{r}(\theta^1, \theta^2, \theta^3)$ are parametrised in terms of the convective coordinates $\{\theta^1, \theta^2, \theta^3\}$ as

$$\mathbf{R}(\theta^1, \theta^2, \theta^3) = \mathbf{X}(\theta^1) + \theta^2 \mathbf{A}_2(\theta^1) + \theta^3 \mathbf{A}_3(\theta^1), \quad (1a)$$

$$\mathbf{r}(\theta^1, \theta^2, \theta^3) = \mathbf{x}(\theta^1) + \theta^2 \mathbf{a}_2(\theta^1) + \theta^3 \mathbf{a}_3(\theta^1), \quad (1b)$$

where $\mathbf{X}(\theta^1)$ and $\mathbf{x}(\theta^1)$ denote the lines of centroids parameterised by θ^1 , see Figure 1. In turn, the cross-section with the radius r is parameterised by $|\theta^2| \leq r$ and $|\theta^3| \leq r$. The tangent vectors to the line of centroids are given by

$$\mathbf{A}_1 = \frac{d\mathbf{X}}{d\theta^1} = \mathbf{X}_{,1}, \quad \mathbf{a}_1 = \frac{d\mathbf{x}}{d\theta^1} = \mathbf{x}_{,1}. \quad (2)$$

The two orthonormal directors \mathbf{A}_2 and \mathbf{A}_3 are chosen so that they satisfy in the reference configuration

$$|\mathbf{A}_l| = 1, \quad \mathbf{A}_2 \cdot \mathbf{A}_3 = 0, \quad \mathbf{A}_1 \cdot \mathbf{A}_l = 0. \quad (3)$$

Here and in the following Greek indices take the values $\{2, 3\}$ and summation over repeated indices is assumed. The two orthonormal directors \mathbf{a}_ι in the deformed configuration are obtained by rotating the reference configuration directors with a rotation matrix $\mathbf{\Lambda} \in \text{SO}_3$,

$$\mathbf{a}_\iota = \mathbf{\Lambda} \mathbf{A}_\iota. \quad (4)$$

This, in combination with the Euler-Bernoulli assumption, ensures that the two directors \mathbf{a}_2 and \mathbf{a}_3 in the deformed configuration satisfy

$$|\mathbf{a}_\iota| = 1, \quad \mathbf{a}_2 \cdot \mathbf{a}_3 = 0, \quad \mathbf{a}_1 \cdot \mathbf{a}_\iota = 0. \quad (5)$$

The rotation $\mathbf{\Lambda}$ is composed of two rotations,

$$\mathbf{\Lambda}(\mathbf{x}, \vartheta) = \mathbf{\Lambda}_2(\mathbf{x}) \mathbf{\Lambda}_1(\vartheta). \quad (6)$$

That is, the reference directors \mathbf{A}_ι are mapped to the deformed directors \mathbf{a}_ι in two steps using an intermediary configuration with $\mathbf{a}'_\iota = \mathbf{\Lambda}_1(\vartheta) \mathbf{A}_\iota$. The matrix $\mathbf{\Lambda}_1(\vartheta)$ describes a rotation by an angle ϑ about the unit tangent $\hat{\mathbf{A}}_1 = \mathbf{A}_1/|\mathbf{A}_1|$ and is according to the Rodrigues formula given by

$$\mathbf{\Lambda}_1(\vartheta) = \mathbf{I} + \sin \vartheta \mathbf{L} + (1 - \cos \vartheta) \mathbf{L} \mathbf{L} \quad (7)$$

with the identity matrix \mathbf{I} and the skew-symmetric matrix

$$\mathbf{L} = \begin{pmatrix} 0 & -\hat{\mathbf{A}}_1 \cdot \mathbf{e}_3 & \hat{\mathbf{A}}_1 \cdot \mathbf{e}_2 \\ \hat{\mathbf{A}}_1 \cdot \mathbf{e}_3 & 0 & -\hat{\mathbf{A}}_1 \cdot \mathbf{e}_1 \\ -\hat{\mathbf{A}}_1 \cdot \mathbf{e}_2 & \hat{\mathbf{A}}_1 \cdot \mathbf{e}_1 & 0 \end{pmatrix}. \quad (8)$$

Subsequently, we use the smallest rotation formula [28, 38] for the second matrix $\mathbf{\Lambda}_2(\mathbf{a}_1)$, which maps $\hat{\mathbf{A}}_1$ to the unit tangent vector $\hat{\mathbf{a}}_1 = \mathbf{a}_1/|\mathbf{a}_1|$,

$$\mathbf{\Lambda}_2(\mathbf{a}_1) = \mathbf{I} - \frac{(\hat{\mathbf{A}}_1 + \hat{\mathbf{a}}_1) \otimes \hat{\mathbf{a}}_1}{1 + \hat{\mathbf{a}}_1 \cdot \hat{\mathbf{A}}_1}. \quad (9)$$

To derive the strains corresponding to the assumed kinematics (1), we consider the Green-Lagrange strain tensor of 3D elasticity

$$\mathbf{E} = E_{ij} \mathbf{G}^i \otimes \mathbf{G}^j = \frac{1}{2}(g_{ij} - G_{ij}) \mathbf{G}^i \otimes \mathbf{G}^j. \quad (10)$$

Here and in the following Latin indices take the values $\{1, 2, 3\}$. The covariant basis vectors \mathbf{G}_i and \mathbf{g}_i and the contravariant basis vectors \mathbf{G}^i and \mathbf{g}^i are defined as

$$\mathbf{G}_i = \frac{\partial \mathbf{R}}{\partial \theta^i}, \quad \mathbf{g}_i = \frac{\partial \mathbf{r}}{\partial \theta^i}, \quad \mathbf{G}_i \cdot \mathbf{G}^j = \delta_i^j, \quad \mathbf{g}_i \cdot \mathbf{g}^j = \delta_i^j, \quad (11)$$

where δ_i^j is the Kronecker delta. The corresponding two metric tensors G_{ij} and g_{ij} are given by

$$G_{ij} = \mathbf{G}_i \cdot \mathbf{G}_j, \quad g_{ij} = \mathbf{g}_i \cdot \mathbf{g}_j. \quad (12)$$

After introducing the assumed kinematics (1) in (10) and some algebraic simplifications we obtain for the components of the strain tensor

$$[E_{ij}] = \begin{bmatrix} \alpha + \theta^2 \beta_2 + \theta^3 \beta_3 & \theta^3 \gamma & -\theta^2 \gamma \\ \text{symmetric} & 0 & 0 \\ & & 0 \end{bmatrix} \quad (13a)$$

with

$$\alpha(\mathbf{x}) = \frac{1}{2}(\mathbf{a}_1 \cdot \mathbf{a}_1 - \mathbf{A}_1 \cdot \mathbf{A}_1), \quad (13b)$$

$$\beta_2(\mathbf{x}, \vartheta) = \mathbf{A}_2 \cdot \mathbf{A}_{1,1} - \mathbf{a}_2 \cdot \mathbf{a}_{1,1}, \quad (13c)$$

$$\beta_3(\mathbf{x}, \vartheta) = \mathbf{A}_3 \cdot \mathbf{A}_{1,1} - \mathbf{a}_3 \cdot \mathbf{a}_{1,1}, \quad (13d)$$

$$\gamma(\mathbf{x}, \vartheta) = \frac{1}{2}(\mathbf{a}_2 \cdot \mathbf{a}_{3,1} - \mathbf{A}_2 \cdot \mathbf{A}_{3,1}). \quad (13e)$$

We identify α , β_2 , β_3 and γ as the membrane, bending about \mathbf{a}_2 , bending about \mathbf{a}_3 and torsional shear strains, respectively. Moreover, due to the Euler-Bernoulli assumption the strain components E_{23} , E_{32} and E_{33} are zero and the in-plane shear strains E_{12} and E_{13} are induced only by torsional shear strain γ .

2.2. Equilibrium equations in weak form

The potential energy of a rod with the line of centroids $\Gamma \subset \mathbb{R}$ and the cross-section $\Omega \subset \mathbb{R}^2$ occupying the volume $V = \Gamma \times \Omega \subset \mathbb{R}^3$ in its reference configuration takes the form

$$\Pi(\mathbf{r}) = \Pi_{\text{int}}(\mathbf{r}) + \Pi_{\text{ext}}(\mathbf{r}) = \int_V \psi(\mathbf{E}) \, dV + \Pi_{\text{ext}}(\mathbf{r}), \quad (14)$$

where $\psi(\mathbf{E})$ is the strain energy density and $\Pi_{\text{ext}}(\mathbf{r})$ is the potential of the externally applied forces. At equilibrium the potential energy of the rod is stationary, i.e.,

$$\delta\Pi(\mathbf{r}) = \delta\Pi_{\text{int}}(\mathbf{r}) + \delta\Pi_{\text{ext}}(\mathbf{r}) = 0 \quad (15a)$$

with the external virtual work $\delta\Pi_{\text{ext}}(\mathbf{r})$ and the internal virtual work

$$\delta\Pi_{\text{int}}(\mathbf{r}) = \int_V \frac{\partial\psi(\mathbf{E})}{\partial\mathbf{E}} : \delta\mathbf{E} \, dV = \int_V \mathbf{S} : \delta\mathbf{E} \, dV, \quad (15b)$$

where \mathbf{S} is the second Piola-Kirchhoff stress tensor. The strain tensor of the rod (13) depends on the displacement of the line of centroids

$$\mathbf{u}(\theta^1) = \mathbf{x}(\theta^1) - \mathbf{X}(\theta^1), \quad (16)$$

and the rotation angle ϑ . Hence, we can write for the internal virtual work (15b) more succinctly

$$\delta\Pi_{\text{int}}(\mathbf{x}) = \int_{\Gamma} \int_{\Omega} \mathbf{S} : \frac{\partial\mathbf{E}}{\partial\mathbf{u}} \cdot \delta\mathbf{u}|_{\mathbf{A}_1} \, d\Omega \, d\Gamma + \int_{\Gamma} \int_{\Omega} \mathbf{S} : \frac{\partial\mathbf{E}}{\partial\vartheta} \delta\vartheta|_{\mathbf{A}_1} \, d\Omega \, d\Gamma \quad (17a)$$

$$= \int_{\Gamma} \mathbf{f}_{\mathbf{u}} \cdot \delta\mathbf{u}|_{\mathbf{A}_1} \, d\Gamma + \int_{\Gamma} f_{\vartheta} \delta\vartheta|_{\mathbf{A}_1} \, d\Gamma, \quad (17b)$$

where $\mathbf{f}_{\mathbf{u}}$ and f_{ϑ} are the internal forces conjugate to the virtual displacements $\delta\mathbf{u}$ and rotations $\delta\vartheta$.

As a material model we use the isotropic St Venant-Kirchhoff model with the strain energy density

$$\psi(\mathbf{E}) = \frac{1}{2} \mathbf{E} : \mathbf{C} : \mathbf{E} = \frac{1}{2} \mathbf{S} : \mathbf{E}, \quad (18)$$

and the fourth-order constitutive tensor

$$\mathbf{C} = C^{ijkl} \mathbf{G}_i \otimes \mathbf{G}_j \otimes \mathbf{G}_k \otimes \mathbf{G}_l = [\lambda G^{ij} G^{kl} + \mu(G^{ik} G^{jl} + G^{il} G^{jk})] \mathbf{G}_i \otimes \mathbf{G}_j \otimes \mathbf{G}_k \otimes \mathbf{G}_l, \quad (19)$$

where λ and μ are the two Lamé parameters [39]. The contravariant metric tensor G^{ij} is determined from the relation $G_{ki}G^{ij} = \delta_k^j$.

To derive analytical expressions for the internal forces we first introduce the rod strain tensor (13) and the constitutive equation (19) in the internal virtual work (17). Subsequently, we integrate over the rod cross-section analytically to obtain the internal forces

$$\mathbf{f}_u = n \frac{\partial \alpha}{\partial \mathbf{u}} + m_2 \frac{\partial \beta_2}{\partial \mathbf{u}} + m_3 \frac{\partial \beta_3}{\partial \mathbf{u}} + q \frac{\partial \gamma}{\partial \mathbf{u}}, \quad (20a)$$

$$f_\vartheta = m_2 \frac{\partial \beta_2}{\partial \vartheta} + m_3 \frac{\partial \beta_3}{\partial \vartheta} + q \frac{\partial \gamma}{\partial \vartheta}. \quad (20b)$$

Here, the axial force n , the bending moments m_l and the torque q are defined as

$$n = EG^{11}G^{11}A\alpha, \quad (21a)$$

$$m_l = EG^{11}G^{11}I_l\beta_l, \quad (21b)$$

$$q = 2EG^{11}J\gamma, \quad (21c)$$

where $A = \pi r^2$, $I_l = \pi r^4/4$ and $J = \pi r^4/2$ are the cross-section area, second moment of area and torsional constant of the circular rod, and E is its Young's modulus. The tedious but straightforward derivation of internal forces and their derivatives are summarised in Appendix A.

2.3. Finite element discretisation

We follow the isogeometric analysis paradigm and use univariate cubic B-splines to discretise the lines of centroids $\mathbf{X}(\theta^1)$ and $\mathbf{x}(\theta^1)$ in the reference and deformed configurations. We choose smooth B-splines because the bending strains β_l in (13) require at least C^1 continuous smooth basis functions. The kinematic relationship (16) is restated after discretisation as

$$\sum_{I=1}^{n_B} B^I(\theta^1)\mathbf{x}_I = \sum_{I=1}^{n_B} B^I(\theta^1)\mathbf{X}_I + \sum_{I=1}^{n_B} B^I(\theta^1)\mathbf{u}_I, \quad (22)$$

where the B-spline basis $B^I(\theta^1)$ and their coefficients correspond to the n_B control vertices on the discretised rod centreline.

The discretised weak form of the equilibrium equations (15) yields after linearisation an algebraic system of equations, which we solve with the Newton-Raphson scheme. For linearisation the gradients of the internal forces (20) are required, see Appendix A.2.

2.4. Yarn-to-yarn contact

We use the Lagrange multiplier method to consider pointwise non-frictional contact between two circular rods. By closely following Wriggers et al. [40] and Weeger et al. [41], we add to the total potential energy $\Pi(\mathbf{r})$ in (14) the contact potential energy

$$\Pi_c(\mathbf{r}) = \tau g_N, \quad (23)$$

where the Lagrange multiplier τ represents the repulsive normal force between the two rods, and the non-positive gap function g_N depends on the minimum distance between the two rods. The distance between the lines of centroids of the two rods $\mathbf{x}^l(\theta_l^1)$ and $\mathbf{x}^r(\theta_r^1)$ is given by

$$d(\theta_l^1, \theta_r^1) = |\mathbf{x}^l(\theta_l^1) - \mathbf{x}^r(\theta_r^1)|, \quad (24)$$

and its minimum by

$$d_{\min} = \min_{\theta_l^1, \theta_r^1} d(\theta_l^1, \theta_r^1) = d(\theta_l^{1c}, \theta_r^{1c}). \quad (25)$$

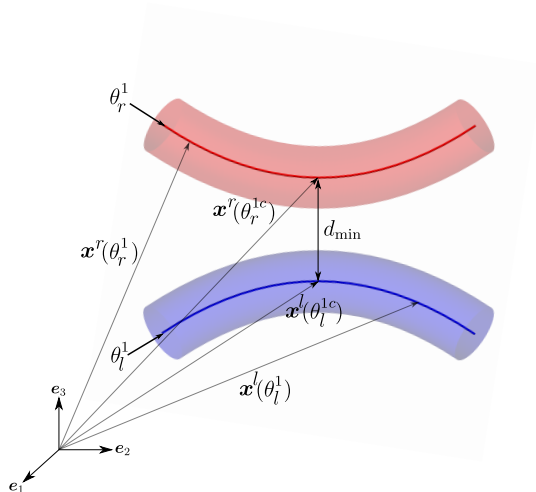


Figure 2. Contact between two rods with the lines of centroids $\mathbf{x}^l(\theta_l^1)$ and $\mathbf{x}^r(\theta_r^1)$. Between the points $\mathbf{x}^l(\theta_l^{1c})$ and $\mathbf{x}^r(\theta_r^{1c})$ the distance is minimum and has the value d_{\min} .

This minimum can be determined using the Newton-Raphson scheme. Ultimately, the non-positive gap function g_N is defined as

$$g_N = \begin{cases} d_{\min} - 2r & d_{\min} < 2r , \\ 0 & d_{\min} \geq 2r , \end{cases} \quad (26)$$

where r is the radius of the rods.

The first variation of the contact potential energy (23) gives its contribution to the weak form of the equilibrium equations (15). This contribution takes the form

$$\delta\Pi_c = \tau\delta g_N + \delta\tau g_N . \quad (27)$$

For further details on our contact implementation we refer to Herath [42].

2.5. Verification of the rod model

We consider a membrane-bending-torsion interaction problem to verify the accuracy of the presented rod formulation. A spatial helicoidal spring is clamped at one end and a vertical load of magnitude 25 kN is applied at the other end, see Figure 3a. The reference geometry of the line of the centroids is given by

$$\mathbf{X}(\theta^1) = \{10 \sin(2\pi \theta^1), 10 \cos(2\pi \theta^1), 20 \theta^1\}, \quad \theta^1 \in [0, 1]. \quad (28)$$

The material and geometric properties of the spring including the reference director orientations \mathbf{A}_i are given in Figure 3a. The tip load is increased from zero to 25 kN in 10 uniform load steps. In Figure 3b the deflected shapes for five different load levels are shown. As can be seen in Figure 4 the obtained tip displacements are in excellent agreement with the results presented in Bauer et al. [29], in which a slightly different approach was used to parameterise the rotations of the two rod directors \mathbf{A}_i .

3. COMPUTATIONAL HOMOGENISATION

3.1. Microscale analysis

A characteristic representative volume element (RVE) as depicted in Figure 5 is chosen to represent the periodic microstructure of a weft-knitted membrane. The intricate spatial

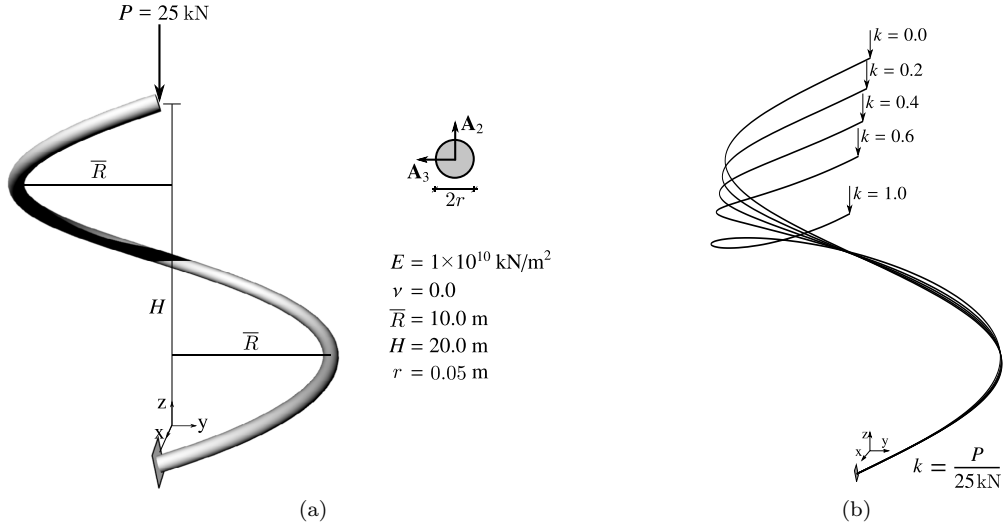


Figure 3. One-sided clamped helicoidal spring with tip loading. Problem description (a) and deformed shapes under different loads (b).

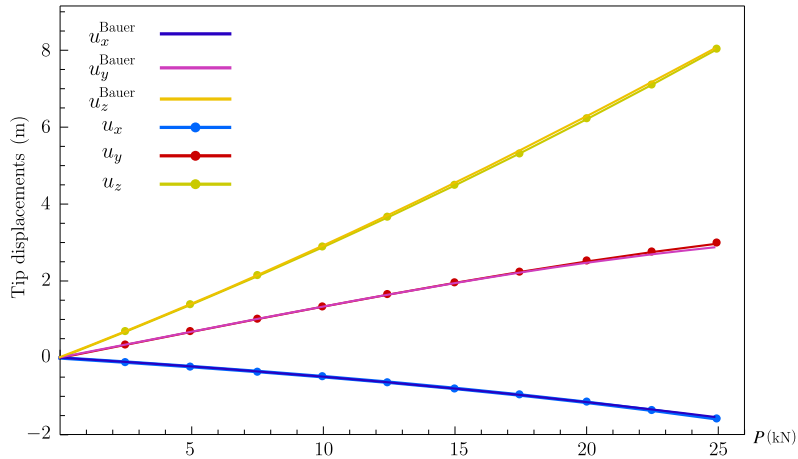


Figure 4. Comparison of the obtained tip displacements of the helicoidal spring with Bauer et al. [29].

arrangement of the yarns in the RVE is modelled, as in recent works [43, 44], using the approximate geometry proposed by Vassiliadis et al. [45], see Appendix B. For alternative geometric descriptions see [46] and references therein. First the yarn centrelines are defined and then the yarns are generated by sweeping a circle along those lines. On the macroscale we model the membrane with subdivision shell finite elements [33, 36, 37] and consider for homogenisation only the in-plane membrane response. The very small out-of-plane bending stiffness contribution of the rods to the membrane bending stiffness is not taken into account.

In first-order homogenisation, the macroscale membrane deformation gradient \mathbf{F}_M is used to define the boundary conditions on the RVE. Here and in the following the macroscale and microscale quantities are denoted by subscripts M and m , respectively. It is assumed that the volume averaged deformation gradient \mathbf{F}_m of the rod in the RVE and the membrane deformation gradient \mathbf{F}_M are equal, that is,

$$\mathbf{F}_M = \frac{1}{V_{RVE}} \int_{V_m} \mathbf{F}_m dV, \quad (29)$$

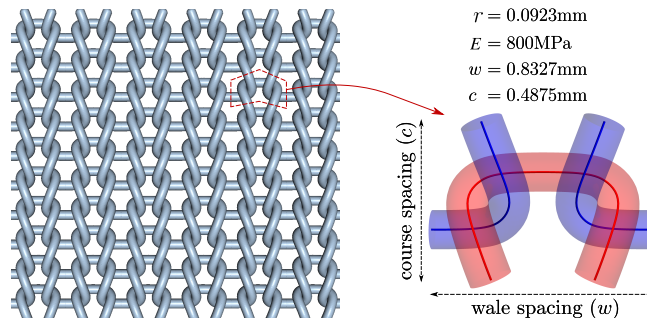


Figure 5. Characteristic weft-knitted RVE selection and the definition of fibre geometric and material parameters.

where V_{RVE} is the RVE volume and V_m is the rod volume within the RVE in the reference configuration. Without going into details, the deformation gradient $\mathbf{F}_m = \partial \mathbf{x} / \partial \mathbf{X}$ of the line of centroids is given by the kinematic assumption (1). The Hill-Mandel lemma states that the macroscale and microscale work for an RVE must be equal

$$\mathbf{P}_M : \mathbf{F}_M = \frac{1}{V_{RVE}} \int_{V_m} \mathbf{P}_m : \mathbf{F}_m \, dV, \quad (30)$$

where \mathbf{P}_M is the macroscale first Piola-Kirchhoff membrane stress and \mathbf{P}_m is the microscale first Piola-Kirchhoff rod stress. The integral represents the internal virtual work of the rod within the RVE and is given by (17). For the lemma (30) to hold only certain types of RVE boundary conditions can be chosen, including Dirichlet and periodic; see [10, 47] for details. Moreover, as a consequence of this lemma the macroscopic first Piola-Kirchhoff stress \mathbf{P}_M can be obtained from the volume averaged internal energy density

$$\mathbf{P}_M = \frac{\partial \psi_M(\mathbf{F}_M)}{\partial \mathbf{F}_M} \quad (31a)$$

with

$$\psi_M(\mathbf{F}_M) = \inf_{\mathbf{F}_m \in \mathcal{K}} \frac{1}{V_{RVE}} \int_{V_m} \psi_m(\mathbf{F}_m) \, dV, \quad (31b)$$

where the set \mathcal{K} denotes the deformation gradients satisfying the RVE boundary conditions. The microscopic energy density ψ_m of a rod with an isotropic St Venant-Kirchhoff material is given by (18).

In this work we choose as RVE boundary conditions the periodic boundary conditions depicted in Figure 6. Due to the orthotropy of the RVE response, the biaxial stretching and shear response are decoupled. Therefore, we consider the two cases separately and choose for each different boundary conditions. Boundary displacements in the thickness direction \mathbf{e}_3 are zero to simulate plane stress conditions.

3.2. Verification and validation of the microscale model

To verify and validate our microscale model we consider RVEs under wale-wise and coarse-wise uniaxial tension and shear as reported in Dinh et al. [43] and Weeger et al. [44]. For a detailed problem description we refer to [43] and [44]. In our computations the yarn is discretised with 128 rod finite elements. In Dinh et al. [43] the yarn is modelled as a 3D solid and in Weeger et al. [44] as a discretised Euler-Bernoulli rod with the collocation method. As evident from Figure 7 our results are in excellent agreement with the experimental and computational results obtained with other approaches. Throughout this paper, we use the yarn geometry and material parameters given in the above-mentioned two papers.

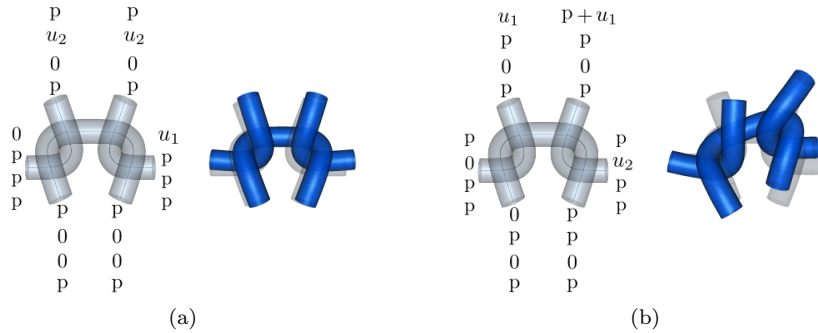


Figure 6. Prescribed periodic boundary conditions and the respective deformed configuration of an RVE subjected to biaxial tension (a) and shear (b). At the six boundary finite element nodes, the four labels describe the boundary conditions for the three displacements and the one rotation, i.e. $(u_1, u_2, u_3, \vartheta)$, where u_i refers to the applied displacements in the e_i direction. The labels p and 0 denote periodic and zero displacement or twist constraints, respectively.

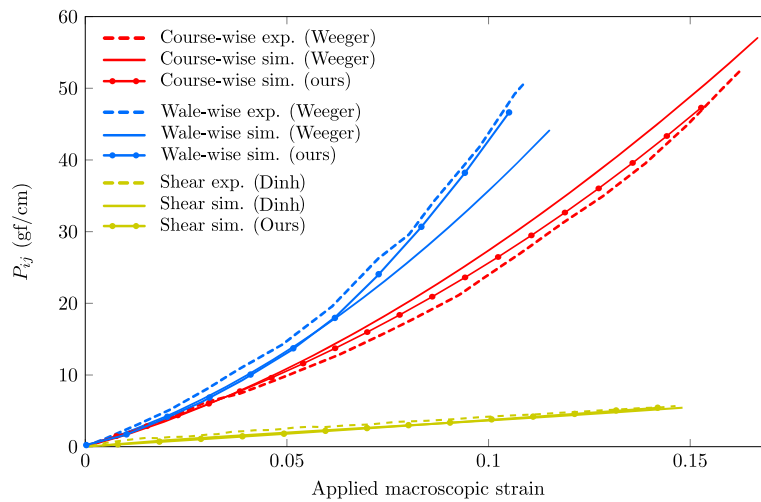


Figure 7. Comparison of the obtained homogenised stresses for an RVE under course-wise and wale-wise uniaxial tension and pure shear with the experimental and numerical results reported in Weeger et al. [44] and Dinh et al. [43]. The unit conversion for stresses is $1.00 \text{ N/mm} = 1019.716213 \text{ gf/cm}$.

4. DATA-DRIVEN HOMOGENISATION

4.1. Review of Gaussian process regression

Gaussian process regression is a statistical inference method rooted in Bayesian statistical learning. In the following, we briefly review the key steps in Gaussian process regression. For further details we refer to Rasmussen et al. [22]. To begin with, we assume as a prior in the Bayesian formulation a random function $f(\mathbf{z})$ given by the zero-mean Gaussian process

$$f(\mathbf{z}) \sim \mathcal{GP}(0, k(\mathbf{z}, \mathbf{z}')) . \quad (32)$$

The respective covariance function $k(\mathbf{z}, \mathbf{z}')$ is chosen to be the (stationary and isotropic) squared exponential function

$$k(\mathbf{z}, \mathbf{z}') = \sigma_f^2 \exp\left(-\frac{(\mathbf{z} - \mathbf{z}')^\top (\mathbf{z} - \mathbf{z}')}{2\ell^2}\right) , \quad (33)$$

where σ_f and ℓ are the yet to be determined scaling and characteristic lengthscale hyperparameters. For convenience, we define $\Theta = (\sigma_f, \ell)$ as the vector of hyperparameters. The infinitely smooth covariance function (33) encodes our prior assumptions about $f(\mathbf{z})$ before observing any training data. Other choices are possible, see [22, Chapter 4].

Next, we consider a database comprised of a known training dataset and testing points. Each data point is given by an input vector \mathbf{z}_i and a corresponding scalar observation y_i , with $i = 1, 2, \dots, n_{GP}$. All training data points are collected in (\mathbf{Z}, \mathbf{y}) and all testing data points with unknown \mathbf{y}_* in $(\mathbf{Z}_*, \mathbf{y}_*)$. Moreover, we define the covariance matrix \mathbf{K} with the components $K_{ij} = k(\mathbf{z}_i, \mathbf{z}_j)$. The discretisation of the Gaussian process (32) for the considered training and test data is given by the multivariate Gaussian distribution

$$\begin{bmatrix} \mathbf{y} \\ \mathbf{y}_* \end{bmatrix} \sim \mathcal{N} \left(\mathbf{0}, \begin{bmatrix} \mathbf{K}(\mathbf{Z}, \mathbf{Z}) & \mathbf{K}(\mathbf{Z}, \mathbf{Z}_*) \\ \mathbf{K}(\mathbf{Z}_*, \mathbf{Z}) & \mathbf{K}(\mathbf{Z}_*, \mathbf{Z}_*) \end{bmatrix} \right). \quad (34)$$

The probability density of the unknown data \mathbf{y}_* at the given locations \mathbf{Z}_* conditioned on the known training data (\mathbf{Z}, \mathbf{y}) reads

$$\mathbf{y}_* | \mathbf{Z}_*, \mathbf{Z}, \mathbf{y} \sim \mathcal{N} \left(\mathbf{K}(\mathbf{Z}_*, \mathbf{Z}) \mathbf{K}(\mathbf{Z}, \mathbf{Z})^{-1} \mathbf{y}, \mathbf{K}(\mathbf{Z}_*, \mathbf{Z}_*) - \mathbf{K}(\mathbf{Z}_*, \mathbf{Z}) \mathbf{K}(\mathbf{Z}, \mathbf{Z})^{-1} \mathbf{K}(\mathbf{Z}, \mathbf{Z}_*) \right). \quad (35)$$

Hence, the best estimate for \mathbf{y}_* is given by the expectation

$$\bar{\mathbf{y}}_* = \mathbf{K}(\mathbf{Z}_*, \mathbf{Z}) \mathbf{K}(\mathbf{Z}, \mathbf{Z})^{-1} \mathbf{y}, \quad (36)$$

and the uncertainty of the estimate $\bar{\mathbf{K}}_*$ is given by the covariance matrix

$$\text{cov}(\mathbf{y}_*) = \mathbf{K}(\mathbf{Z}_*, \mathbf{Z}_*) - \mathbf{K}(\mathbf{Z}_*, \mathbf{Z}) \mathbf{K}(\mathbf{Z}, \mathbf{Z})^{-1} \mathbf{K}(\mathbf{Z}, \mathbf{Z}_*). \quad (37)$$

The covariance matrix $\mathbf{K}(\mathbf{Z}, \mathbf{Z})$ of size $n_{GP} \times n_{GP}$ is dense for the covariance kernel (33). If the number of training points n_{GP} become too large to invert $\mathbf{K}(\mathbf{Z}, \mathbf{Z})$, alternative approaches leading to sparse covariance matrices need to be considered [22, Chapter 8].

To estimate the hyperparameters Θ , we consider the marginal likelihood, or the evidence,

$$p(\mathbf{y} | \mathbf{Z}) = \int p(\mathbf{y} | \mathbf{Z}, \mathbf{f}) p(\mathbf{f} | \mathbf{Z}) d\mathbf{f}, \quad (38)$$

with the likelihood $p(\mathbf{y} | \mathbf{Z}, \mathbf{f})$ and the prior $p(\mathbf{f} | \mathbf{Z}) = \mathcal{N}(\mathbf{0}, \mathbf{K}(\mathbf{Z}, \mathbf{Z}))$, where \mathbf{f} are function values evaluated at \mathbf{Z} , c.f. (32). The marginal likelihood is the probability of observing the data \mathbf{y} for given hyperparameters Θ . Hence, it suggests itself to choose the hyperparameters so that the probability observing the given training data \mathbf{y} is maximised. In practice, it is numerically more stable to compute the maximum of the log marginal likelihood given by

$$\log p(\mathbf{y} | \mathbf{Z}) = -\frac{1}{2} \mathbf{y}^\top \mathbf{K}^{-1} \mathbf{y} - \frac{1}{2} \log |\mathbf{K}| - \frac{n_{GP}}{2} \log 2\pi. \quad (39)$$

Note that the log is a monotonic function so that

$$\Theta^* = \arg \max_{\Theta} p(\mathbf{y} | \mathbf{Z}) = \arg \max_{\Theta} (\log p(\mathbf{y} | \mathbf{Z})). \quad (40)$$

We use the scikit-learn Python library [48] to find Θ^* with a gradient-based optimisation algorithm. The marginal likelihood is a non-convex function and certain care has to be taken to find the global maximum. After the optimal hyperparameters are determined they are used in computing the mean (36) and covariance (37).

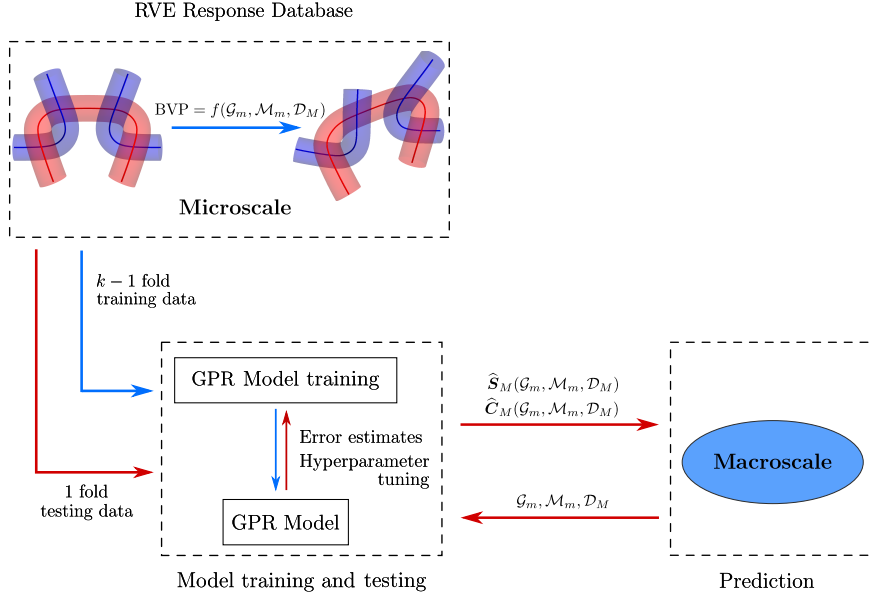


Figure 8. Data-driven computational homogenisation and material design framework using Gaussian process regression.

4.2. Gaussian process homogenisation

The implemented data-driven homogenisation framework is illustrated in Figure 8 and closely follows Bessa et al. [16]. Data-driven homogenisation begins with constructing a response database for the RVE. This response database is designed by defining the microscale boundary value problem (BVP) using three types of design variables, namely geometric properties \mathcal{G}_m , material properties \mathcal{M}_m and boundary conditions \mathcal{D}_M . In this paper, we concentrate on the design variable \mathcal{D}_M relevant to homogenisation. It is straightforward to include \mathcal{G}_m and \mathcal{M}_m which lead to the material design of knitted membranes.

Next, we determine the hyperparameters of the GPR model using k -fold cross-validation rather than directly using the Θ^* obtained with (40) considering the entire training dataset. The GPR model is iteratively evaluated by using $k-1$ folds for training and the remaining one for testing. We choose $k=5$ which provides a good compromise between accuracy and efficiency. As error metrics for the predicted strain energy and stress resultants we use the correlation of determination \mathcal{R}^2 and the mean squared error (MSE) given by

$$\mathcal{R}^2(\mathbf{y}, \hat{\mathbf{y}}) = 1 - \frac{\sum_{i=1}^{n_T} (y_i - \hat{y}_i)^2}{\sum_{i=1}^{n_T} (y_i - \bar{y})^2}, \quad (41a)$$

$$\text{MSE}(\mathbf{y}, \hat{\mathbf{y}}) = \frac{1}{n_T} \sum_{i=1}^{n_T} (y_i - \hat{y}_i)^2, \quad (41b)$$

where $n_T = \lfloor n_{GP}/(k-1) \rfloor$ is the number of the test points, \mathbf{y} is the target output, $\hat{\mathbf{y}}$ is the predicted output and \bar{y} is the expectation of the target output given by the GPR model. When evaluating the MSE of the predicted stress tensor, we take the square root of the squared sum of the MSE of each stress resultant

$$\text{MSE}(\mathbf{S}, \hat{\mathbf{S}}) = \sqrt{\text{MSE}^2(S_{11}, \hat{S}_{11}) + \text{MSE}^2(S_{22}, \hat{S}_{22}) + \text{MSE}^2(S_{12}, \hat{S}_{12})}. \quad (42)$$

The GPR model training is implemented in a Python environment using scikit-learn machine learning library [48]. For each test fold, we determine the corresponding hyperparameters by maximising the log marginal likelihood (40). It is expected that the obtained hyperparameters

have similar values for all test folds. In practice, this is not the case because the log marginal likelihood is usually a non-convex function. Therefore, we vary during optimisation the upper and lower limits of the hyperparameters so that all test folds yield similar hyperparameter values. Once this is achieved, we record the hyperparameters Θ^* of the GPR model, which has the lowest MSE, and save the model for subsequent macroscale analyses.

Lastly, we integrate our in-house thin-shell solver [32, 37] with the trained GPR model to simulate the homogenised knitted membrane. As shown in Figure 8, for given macroscale deformations (strains) the trained GPR model yields the corresponding predicted stress resultants and their tangents to the macroscale shell solver.

4.3. Macroscale analysis

For plane-stress membrane deformation, a response database is created with the three in-plane components of the Green-Lagrange strain \mathbf{E} as the inputs and RVE volume averaged strain energy $\psi(\mathbf{E})$ as the output, i.e. z_i and y_i in Section 4.2. With a slight abuse of notation \mathbf{E} is here, in contrast to Section 2.1, a two-dimensional second order tensor. In the four-dimensional response database, points have the coordinates $(\mathbf{E}, \psi) = (E_{11}, E_{22}, E_{12}, \psi)$. The strain components E_{11} and E_{22} correspond to a biaxial deformation state that is decoupled from the shear deformation state with E_{12} , see Section 3.1. The RVE strain energy ψ is obtained by considering a biaxial strain state with E_{11} and E_{22} and a shear deformation state with E_{12} and summing up their strain energies. We use the validated strain limits of Figure 7 in constructing the response database. Thus, allowing for a 5% compressive strains, we define the design variables of the response database as,

$$\mathcal{D}_M = \begin{cases} \mathcal{D}_M^1 = E_{11} \in [-0.05, 0.15], \\ \mathcal{D}_M^2 = E_{22} \in [-0.05, 0.15], \\ \mathcal{D}_M^3 = E_{12} \in [0.00, 0.15]. \end{cases} \quad (43)$$

We solve the RVE problem with the boundary conditions stipulated by the strain states defined in (43) and store the strain components and respective volume averaged energies in the response database. After passing the GPR model training and testing phase, as shown in Figure 8, the strain energy density ψ of the plane-stress deformation is predicted for a given deformed state of the RVE. Plane stresses and stress tangents are computed by differentiating (36), that is,

$$\hat{\mathbf{S}}_M = \frac{\partial \hat{\psi}_M}{\partial \mathbf{E}_M} \quad \text{and} \quad \hat{\mathbf{C}}_M = \frac{\partial \hat{\mathbf{S}}_M}{\partial \mathbf{E}_M}. \quad (44)$$

5. EXAMPLES

5.1. GPR model training and testing

We start with presenting the error metrics of GPR model training and testing for varied sizes of response databases. GPR model training errors are observed to take values $\mathcal{R}^2 = 1.0$ and $\text{MSE} < 10^{-8}$. Hence, we present only the error metrics of testing datasets. All the following computations are performed on the Intel Core i5-4590 CPU @ 3.30GHz \times 4 processor.

Figure 9 shows the MSEs of predicted energy density and second Piola-Kirchhoff stress resultants, as well as a comparison between two sampling techniques, namely uniform sampling and Sobol sampling [49], on the testing errors. Uniformly sampled data points are generated in a way that for the three features in the input vector \mathbf{z}_i , n_S^3 entries occupy the response database, where n_S is the number of uniformly distributed entries in each feature. In total seven datasets with $n_S^3 \in \{216, 343, 729, 1331, 1728, 2197, 4913, 12167\}$ are considered; 80% of each are taken as training points and the remaining as testing points. Moreover, $\mathcal{R}^2 = 1.0$ is

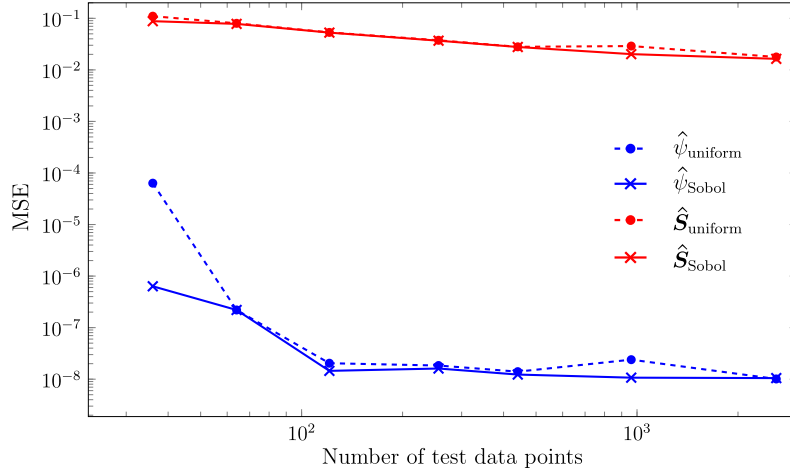


Figure 9. GPR model training and testing. The mean squared error of the predicted strain energy density and the second Piola-Kirchhoff stress resultants for uniform and Sobol sampling.

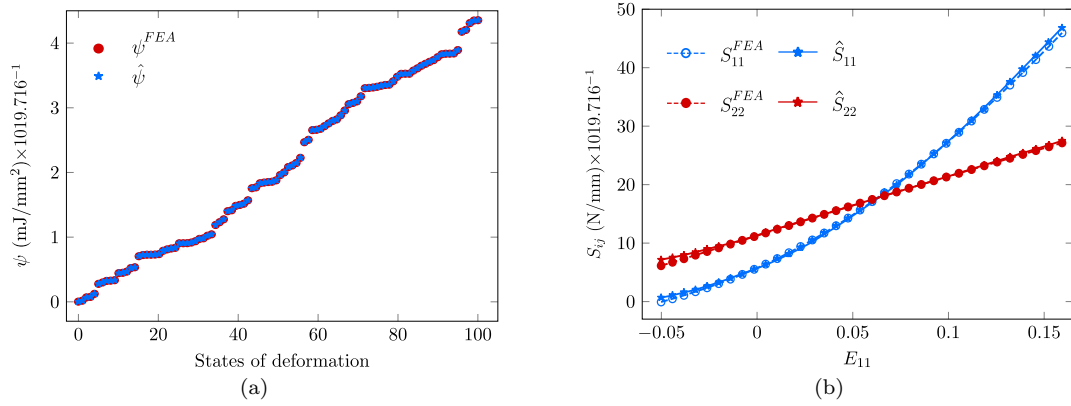


Figure 10. GPR model training and testing. Predictions of (a) strain energy density (sorted by ascending potential) and (b) stress resultants for a biaxial strain state of $E_{11} = [-0.05, 0.15]$, $E_{22} = 0.08$ and $E_{12} = 0$.

rounded to the fifth decimal number for all response databases. MSEs in stress predictions are comparatively higher than those in energy predictions but remain less than 2%. Considering the error convergence and algorithmic efficiency, we use a response database with 2601 test data points in the subsequent macroscale simulations. Furthermore, this particular trained GPR model has the optimum hyperparameter values $\Theta^* = (\sigma_f, \ell) = (1.25213, 0.00904)$ and the maximum log marginal likelihood 9594.98391. Model training time was recorded as 29 minutes and 48 seconds. In Figure 10, we visualise and compare the predictions of a subsample of the chosen response database. Figure 10a depicts the strain energy density predictions, whereas Figure 10b presents the stress predictions for the biaxial homogenised response of an RVE.

5.2. Stretched membrane I: comparison of yarn-level and homogenised displacements

We consider a membrane under uniaxial tension and compare its response using the Gaussian process homogenised material model and an equivalent yarn-level model. The yarn-level model comprises 12 loops in the course direction and 12 loops in the wale direction. We use for the analysis with the homogenised material model a membrane of equal size, that is, 10.00 mm long, 5.85 mm wide and 0.2356 mm thick. The membrane is discretised with a

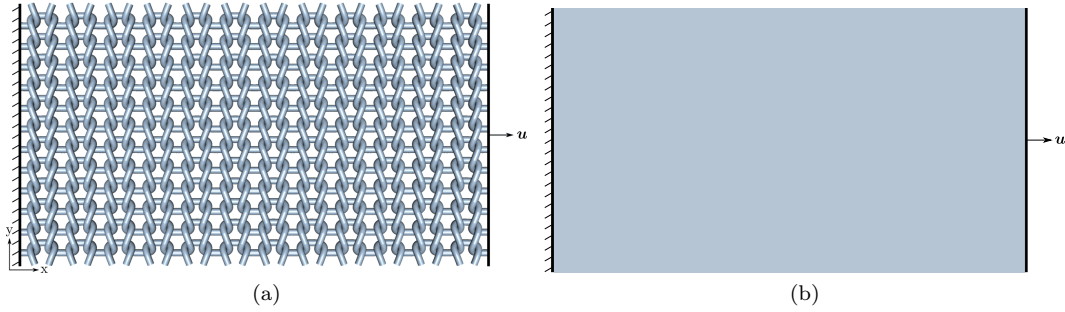


Figure 11. Stretched membrane I. Problem description for the yarn-level (a) and the homogenised membrane (b) models.

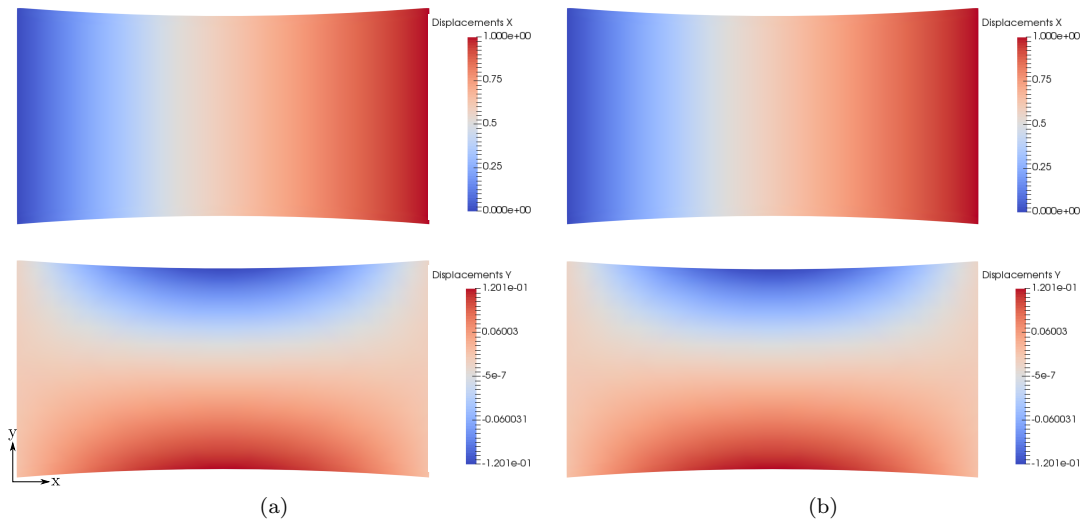


Figure 12. Stretched membrane I. Comparison of horizontal and vertical displacement iso-contours of the yarn-level (a) and homogenised membrane (b) models.

structured quadrilateral mesh with 12×12 elements. Problem descriptions of the two models are presented in Figure 11.

Both models are stretched by 1 mm in the x -direction and the resulting x and y displacements are presented in Figure 12. For comparison purposes, the results of the yarn level model in Figure 12a are visualised by projecting the nodal values of the yarn onto the $x - y$ plane and interpolating them on a Delaunay mesh. The y -direction displacement distribution of the yarn model in Figure 12a is slightly different from that of the homogenised membrane in Figure 12b. This difference has two causes. First, zero out-of-plane displacement boundary conditions on the top and bottom edges of the yarn-level model directly contribute to the observed difference. These boundary conditions are applied to simulate selvedge stitches that restrict the top and bottom yarns from being freely straightened during deformation. Secondly, the geometric asymmetry of the yarn-level model about the mid-horizontal plane has an influence on the overall response due to the relatively small number of loops used in both course and wale directions. Furthermore, a very similar Poisson effect is observed in both the yarn-level and homogenised membrane models. The absolute maximum y -displacement is recorded with 0.12 mm for a stretch by 1 mm in the x -direction.

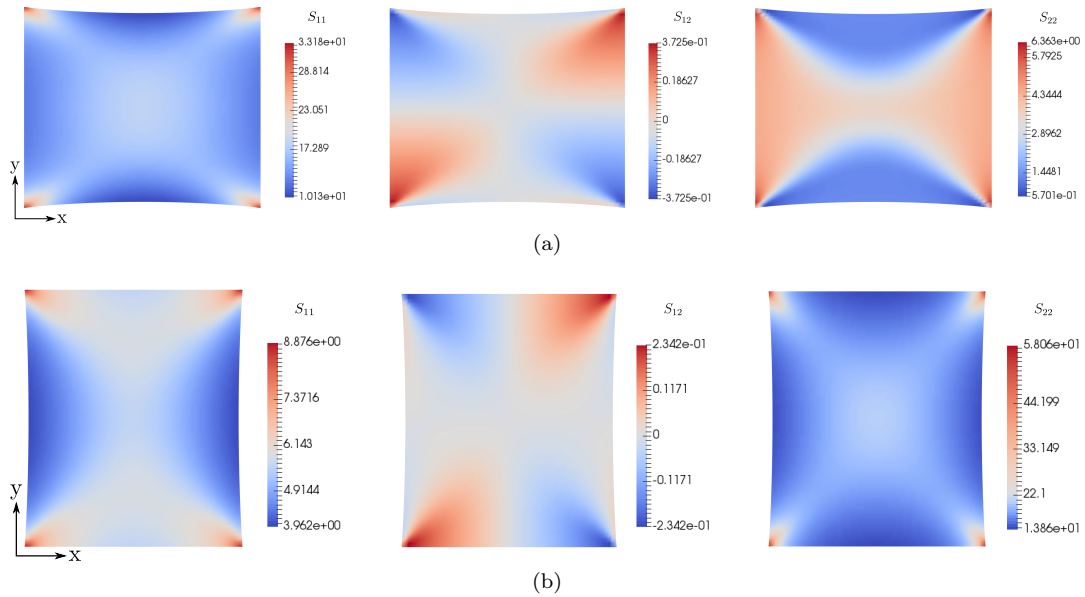


Figure 13. Stretched membrane II: Second Piola-Kirchhoff stress contours of the homogenised course-wise stretched (a) and wale-wise stretched (b) membranes.

5.3. Stretched membrane II: homogenised stresses

We perform two stretch tests on a square knitted membrane sheet with a side length of 10 mm in the course and wale directions. A structured quadrilateral mesh of size 10×10 (100 elements) is used. During the displacement controlled deformation one edge is fixed while the other is stretched in the course or wale direction, respectively, by 1 mm. The deformed shapes and stress contours are depicted in Figure 13a for course-wise and in Figure 13b for wale-wise stretching. Figure 13 clearly shows the orthotropic response of the knitted membrane as the stress resultants are different depending on the direction of the stretching, comparing, e.g., S_{11} in Figure 13a with S_{22} in Figure 13b. Furthermore, the stiffer response in the wale-wise direction manifests itself in a higher stress S_{22} in Figure 13b in comparison to S_{11} in Figure 13a.

6. CONCLUSIONS

We introduced a data-driven approach for computational homogenisation of knitted membranes to address the challenges posed by conventional homogenisation schemes. The inherent large deformations in knitted textiles are accurately captured by the finite deformation rod model and validated against experimental and numerical results. Incorporating the statistical GPR model in computational homogenisation circumvents the need for expensive microscale simulations at each quadrature point of the macroscale membrane, thus yielding significant computational savings.

The presented approach can be extended in several ways. In this paper, we considered only weft-knitted membranes with a uniform stitch pattern. To produce complex three-dimensional surfaces, it is necessary to alter the stitch pattern, for instance, by locally increasing or decreasing the number of loops from row to row or reducing the number of rows. Such changes represent discontinuities in the stitch pattern, and suitable RVEs have to be defined to capture their homogenised response. Putting aside questions of RVE size and validity of homogenisation assumptions, it is straightforward to consider in the introduced data-driven

approach RVEs with other stitch patterns. Furthermore, depending on the loading conditions knitted membranes are prone to geometric instabilities in form of wrinkling on the macroscale and rod buckling on the microscale. In presence of such instabilities the homogenisation assumptions are usually not valid and alternative approaches must be used [50, 51]. The data-driven variants of these approaches are essential for the analysis of large-scale knitted membranes. Finally, a key advantage of the data-driven approach is the prospect to consider design parameters, pertaining to the stitch geometry or yarn material, in the GPR model. This opens up the possibility to optimise those parameters with an efficient gradient-based optimisation algorithm.

A. DERIVATIVES OF STRAINS AND INTERNAL FORCES

In this Appendix we summarise the detailed equations used in the implementation of the introduced finite deformation rod finite element.

A.1. Strain derivatives

The derivative of the components E_{ij} of the strain tensor (13) with respect to the nodal displacements \mathbf{u}_I are given by

$$\frac{\partial \alpha}{\partial \mathbf{u}_I} = \mathbf{a}_1 B_{,1}^I, \quad (45a)$$

$$\frac{\partial \beta_l}{\partial \mathbf{u}_I} = -\frac{\partial \mathbf{a}_l}{\partial \mathbf{u}_I} \cdot \mathbf{a}_{1,1} - \mathbf{a}_l \cdot \frac{\partial \mathbf{a}_{1,1}}{\partial \mathbf{u}_I}, \quad (45b)$$

$$\frac{\partial \gamma}{\partial \mathbf{u}_I} = \frac{1}{2} \left(\frac{\partial \mathbf{a}_2}{\partial \mathbf{u}_I} \cdot \mathbf{a}_{3,1} + \mathbf{a}_2 \cdot \frac{\partial \mathbf{a}_{3,1}}{\partial \mathbf{u}_I} \right), \quad (45c)$$

where

$$\begin{aligned} \frac{\partial \mathbf{a}_1}{\partial \mathbf{u}_I} &= B_{,1}^I \mathbf{I}, \\ \frac{\partial \mathbf{a}_{1,1}}{\partial \mathbf{u}_I} &= B_{,11}^I \mathbf{I}, \\ \frac{\partial \mathbf{a}_l}{\partial \mathbf{u}_I} &= \frac{\partial \Lambda_2}{\partial \mathbf{u}_I} \Lambda_1 \mathbf{A}_l, \\ \mathbf{a}_{l,1} &= \Lambda_{2,1} \Lambda_1 \mathbf{A}_l + \Lambda_2 \Lambda_{1,1} \mathbf{A}_l + \Lambda_2 \Lambda_1 \mathbf{A}_{l,1}, \\ \frac{\partial \mathbf{a}_{l,1}}{\partial \mathbf{u}_I} &= \frac{\partial \Lambda_{2,1}}{\partial \mathbf{u}_I} \Lambda_1 \mathbf{A}_l + \frac{\partial \Lambda_2}{\partial \mathbf{u}_I} \Lambda_{1,1} \mathbf{A}_l + \frac{\partial \Lambda_2}{\partial \mathbf{u}_I} \Lambda_1 \mathbf{A}_{l,1}. \end{aligned}$$

The derivative of the rotation matrix Λ_2 in (9) with respect to the nodal displacements \mathbf{u}_I reads

$$\frac{\partial \Lambda_2}{\partial \mathbf{u}_I} = \frac{\partial \Lambda_2}{\partial \hat{\mathbf{a}}_1} \frac{\partial \hat{\mathbf{a}}_1}{\partial \mathbf{u}_I}, \quad (46)$$

where

$$\begin{aligned} \frac{\partial \Lambda_2}{\partial \hat{\mathbf{a}}_1} &= -\frac{(\hat{\mathbf{A}}_1 + \hat{\mathbf{a}}_1) \otimes \mathbf{I}}{(1 + \hat{\mathbf{a}}_1 \cdot \hat{\mathbf{A}}_1)} - \frac{\mathbf{I} \otimes \hat{\mathbf{a}}_1}{(1 + \hat{\mathbf{a}}_1 \cdot \hat{\mathbf{A}}_1)} + \frac{((\hat{\mathbf{A}}_1 + \hat{\mathbf{a}}_1) \otimes \hat{\mathbf{A}}_1) \otimes \hat{\mathbf{a}}_1}{(1 + \hat{\mathbf{a}}_1 \cdot \hat{\mathbf{A}}_1)^2}, \\ \frac{\partial \hat{\mathbf{a}}_1}{\partial \mathbf{u}_I} &= \left(\frac{\mathbf{I}}{|\mathbf{a}_1|} - \frac{\mathbf{a}_1 \otimes \mathbf{a}_1}{|\mathbf{a}_1|^3} \right) B_{,1}^I. \end{aligned}$$

The derivatives of the bending and torsional shear strains in (13) with respect to the nodal twist ϑ_I are given by

$$\frac{\partial \beta_\ell}{\partial \vartheta_I} = -\frac{\partial \mathbf{a}_\ell}{\partial \vartheta_I} \cdot \mathbf{a}_{1,1}, \quad (47a)$$

$$\frac{\partial \gamma}{\partial \vartheta_I} = \frac{1}{2} \left(\frac{\partial \mathbf{a}_2}{\partial \vartheta_I} \cdot \mathbf{a}_{3,1} + \mathbf{a}_2 \cdot \frac{\partial \mathbf{a}_{3,1}}{\partial \vartheta_I} \right), \quad (47b)$$

where

$$\begin{aligned} \frac{\partial \mathbf{a}_\ell}{\partial \vartheta_I} &= \Lambda_2 \frac{\partial \Lambda_1}{\partial \vartheta_I} \mathbf{A}_\ell, \\ \frac{\partial \mathbf{a}_{\ell,1}}{\partial \vartheta_I} &= \Lambda_{2,1} \frac{\partial \Lambda_1}{\partial \vartheta_I} \mathbf{A}_\ell + \Lambda_2 \frac{\partial \Lambda_{1,1}}{\partial \vartheta_I} \mathbf{A}_\ell + \Lambda_2 \frac{\partial \Lambda_1}{\partial \vartheta_I} \mathbf{A}_{\ell,1}. \end{aligned}$$

The derivative of the rotation matrix Λ_1 in (7) with respect to the nodal twist ϑ_I is given by

$$\frac{\partial \Lambda_1}{\partial \vartheta_I} = \frac{\partial \Lambda_1}{\partial \vartheta} \frac{\partial \vartheta}{\partial \vartheta_I}, \quad (48a)$$

$$\frac{\partial \Lambda_1}{\partial \vartheta} = \cos \vartheta \mathbf{L} + \sin \vartheta \mathbf{L}\mathbf{L}, \quad (48b)$$

where

$$\begin{aligned} \frac{\partial \vartheta}{\partial \vartheta_I} &= B^I, \\ \frac{\partial \Lambda_{1,1}}{\partial \vartheta_I} &= \cos \vartheta \mathbf{L}_{,1} B^I - \sin \vartheta \mathbf{L} \vartheta_{,1} B^I + \cos \vartheta \mathbf{L} B_{,1}^I \\ &\quad + \sin \vartheta (\mathbf{L}\mathbf{L}_{,1} + \mathbf{L}_{,1} \mathbf{L}) B^I + \cos \vartheta \mathbf{L}\mathbf{L} \vartheta_{,1} B^I + \sin \vartheta \mathbf{L}\mathbf{L} \vartheta_{,1} B_{,1}^I. \end{aligned}$$

The second derivatives of the rotation matrix Λ_1 and its derivative $\Lambda_{1,1}$ with respect to the nodal twist ϑ_I are given by

$$\frac{\partial^2 \Lambda_1}{\partial \vartheta_I \partial \vartheta_J} = (-\sin \vartheta \mathbf{L} + \cos \vartheta \mathbf{L}\mathbf{L}) B^I B^J, \quad (49a)$$

$$\begin{aligned} \frac{\partial^2 \Lambda_{1,1}}{\partial \vartheta_I \partial \vartheta_J} &= -\sin \vartheta \mathbf{L}_{,1} B^I B^J - \cos \vartheta \mathbf{L} \vartheta_{,1} B^I B^J - \sin \vartheta \mathbf{L} \vartheta_{,1} B^I B_{,1}^J + (\mathbf{L}\mathbf{L}_{,1} + \mathbf{L}_{,1} \mathbf{L}) \cos \vartheta B^I B^J \\ &\quad - \sin \vartheta \mathbf{L}\mathbf{L} \vartheta_{,1} B^I B^J + \cos \vartheta \mathbf{L}\mathbf{L} B^I B_{,1}^J + \cos \vartheta \mathbf{L}\mathbf{L} B_{,1}^I B^J. \end{aligned} \quad (49b)$$

A.2. Internal force derivatives

We derive next the derivatives of the internal forces needed in computing the stiffness matrix. The derivative of the internal force vector \mathbf{f}_u with respect to the nodal displacements \mathbf{u}_J and the twist ϑ_J are given by

$$\frac{\partial (\mathbf{f}_u)_I}{\partial \mathbf{u}_J} = \frac{\partial n}{\partial \mathbf{u}_J} \frac{\partial \alpha}{\partial \mathbf{u}_I} + n \frac{\partial^2 \alpha}{\partial \mathbf{u}_I \partial \mathbf{u}_J} + \sum_{j=2}^3 \left(\frac{\partial m_j}{\partial \mathbf{u}_J} \frac{\partial \beta_j}{\partial \mathbf{u}_I} + m_j \frac{\partial^2 \beta_j}{\partial \mathbf{u}_I \partial \mathbf{u}_J} \right) + \frac{\partial q}{\partial \mathbf{u}_J} \frac{\partial \gamma}{\partial \mathbf{u}_I} + q \frac{\partial^2 \gamma}{\partial \mathbf{u}_I \partial \mathbf{u}_J}, \quad (50a)$$

$$\frac{\partial (\mathbf{f}_u)_I}{\partial \vartheta_J} = \sum_{j=2}^3 \left(\frac{\partial m_j}{\partial \vartheta_J} \frac{\partial \beta_j}{\partial \mathbf{u}_I} + m_j \frac{\partial^2 \beta_j}{\partial \mathbf{u}_I \partial \vartheta_J} \right) + \frac{\partial q}{\partial \vartheta_J} \frac{\partial \gamma}{\partial \mathbf{u}_I} + q \frac{\partial^2 \gamma}{\partial \mathbf{u}_I \partial \vartheta_J}. \quad (50b)$$

Due to the symmetry of the second derivatives we have

$$\frac{\partial(f_\vartheta)_I}{\partial \mathbf{u}_J} = \left[\frac{\partial(\mathbf{f}_\mathbf{u})_I}{\partial \vartheta_J} \right]^\top, \quad (51)$$

and the derivative of the internal force vector \mathbf{f}_ϑ with respect to the nodal twist ϑ_J is simplified as

$$\frac{\partial(f_\vartheta)_I}{\partial \vartheta_J} = \sum_{j=2}^3 \left(\frac{\partial m_j}{\partial \vartheta_J} \frac{\partial \beta_j}{\partial \vartheta_I} + m_j \frac{\partial^2 \beta_j}{\partial \vartheta_I \partial \vartheta_J} \right) + \frac{\partial q}{\partial \vartheta_J} \frac{\partial \gamma}{\partial \vartheta_I} + q \frac{\partial^2 \gamma}{\partial \vartheta_I \partial \vartheta_J}. \quad (52)$$

The second derivatives of the strains with respect to the nodal displacements \mathbf{u}_I are given by

$$\frac{\partial^2 \alpha}{\partial \mathbf{u}_I \partial \mathbf{u}_J} = \frac{\partial}{\partial \mathbf{u}_J} \left(\mathbf{a}_1 \cdot \frac{\partial \mathbf{a}_1}{\partial \mathbf{u}_I} \right) = \frac{\partial \mathbf{a}_1}{\partial \mathbf{u}_J} \cdot \frac{\partial \mathbf{a}_1}{\partial \mathbf{u}_I}, \quad (53a)$$

$$\begin{aligned} \frac{\partial^2 \beta_\iota}{\partial \mathbf{u}_I \partial \mathbf{u}_J} &= -\frac{\partial}{\partial \mathbf{u}_J} \left(\frac{\partial \beta_\iota}{\partial \mathbf{u}_I} \right) = -\frac{\partial}{\partial \mathbf{u}_J} \left(\frac{\partial \mathbf{a}_\iota}{\partial \mathbf{u}_I} \cdot \mathbf{a}_{1,1} + \mathbf{a}_\iota \cdot \frac{\partial \mathbf{a}_{1,1}}{\partial \mathbf{u}_I} \right) \\ &= -\frac{\partial \mathbf{a}_\iota}{\partial \mathbf{u}_I} \cdot \frac{\partial \mathbf{a}_{1,1}}{\partial \mathbf{u}_J} - \frac{\partial^2 \mathbf{a}_\iota}{\partial \mathbf{u}_I \partial \mathbf{u}_J} \cdot \mathbf{a}_{1,1} - \frac{\partial \mathbf{a}_\iota}{\partial \mathbf{u}_J} \cdot \frac{\partial \mathbf{a}_{1,1}}{\partial \mathbf{u}_I}, \end{aligned} \quad (53b)$$

$$\frac{\partial^2 \mathbf{a}_\iota}{\partial \mathbf{u}_I \partial \mathbf{u}_J} = \frac{\partial}{\partial \mathbf{u}_J} \left(\frac{\partial \Lambda_2}{\partial \mathbf{u}_I} \Lambda_1 \mathbf{A}_\iota \right) = \frac{\partial^2 \Lambda_2}{\partial \mathbf{u}_I \partial \mathbf{u}_J} \Lambda_1 \mathbf{A}_\iota, \quad (53c)$$

$$\begin{aligned} \frac{\partial^2 \gamma}{\partial \mathbf{u}_I \partial \mathbf{u}_J} &= \frac{1}{2} \frac{\partial}{\partial \mathbf{u}_J} \left(\frac{\partial \mathbf{a}_2}{\partial \mathbf{u}_I} \cdot \mathbf{a}_{3,1} + \mathbf{a}_2 \cdot \frac{\partial \mathbf{a}_{3,1}}{\partial \mathbf{u}_I} \right), \\ &= \frac{1}{2} \left(\frac{\partial \mathbf{a}_2}{\partial \mathbf{u}_I} \cdot \frac{\partial \mathbf{a}_{3,1}}{\partial \mathbf{u}_J} + \frac{\partial^2 \mathbf{a}_2}{\partial \mathbf{u}_I \partial \mathbf{u}_J} \cdot \mathbf{a}_{3,1} + \frac{\partial \mathbf{a}_2}{\partial \mathbf{u}_J} \cdot \frac{\partial \mathbf{a}_{3,1}}{\partial \mathbf{u}_I} + \mathbf{a}_2 \cdot \frac{\partial^2 \mathbf{a}_{3,1}}{\partial \mathbf{u}_I \partial \mathbf{u}_J} \right), \end{aligned} \quad (53d)$$

$$\begin{aligned} \frac{\partial^2 \mathbf{a}_{3,1}}{\partial \mathbf{u}_I \partial \mathbf{u}_J} &= \frac{\partial}{\partial \mathbf{u}_J} \left(\frac{\partial \Lambda_{2,1}}{\partial \mathbf{u}_I} \Lambda_1 \mathbf{A}_3 + \frac{\partial \Lambda_2}{\partial \mathbf{u}_I} \Lambda_{1,1} \mathbf{A}_3 + \frac{\partial \Lambda_2}{\partial \mathbf{u}_I} \Lambda_1 \mathbf{A}_{3,1} \right), \\ &= \frac{\partial^2 \Lambda_{2,1}}{\partial \mathbf{u}_I \partial \mathbf{u}_J} \Lambda_1 \mathbf{A}_3 + \frac{\partial^2 \Lambda_2}{\partial \mathbf{u}_I \partial \mathbf{u}_J} \Lambda_{1,1} \mathbf{A}_3 + \frac{\partial^2 \Lambda_2}{\partial \mathbf{u}_I \partial \mathbf{u}_J} \Lambda_1 \mathbf{A}_{3,1}. \end{aligned} \quad (53e)$$

And the mixed second derivatives of the strains are given by

$$\begin{aligned} \frac{\partial^2 \beta_\iota}{\partial \mathbf{u}_I \partial \vartheta_J} &= -\frac{\partial}{\partial \vartheta_J} \left(\frac{\partial \beta_\iota}{\partial \mathbf{u}_I} \right) = -\frac{\partial}{\partial \vartheta_J} \left(\frac{\partial \mathbf{a}_\iota}{\partial \mathbf{u}_I} \cdot \mathbf{a}_{1,1} + \mathbf{a}_\iota \cdot \frac{\partial \mathbf{a}_{1,1}}{\partial \mathbf{u}_I} \right) \\ &= -\frac{\partial^2 \mathbf{a}_\iota}{\partial \mathbf{u}_I \partial \vartheta_J} \cdot \mathbf{a}_{1,1} - \frac{\partial \mathbf{a}_\iota}{\partial \vartheta_J} \cdot \frac{\partial \mathbf{a}_{1,1}}{\partial \mathbf{u}_I}, \end{aligned} \quad (54a)$$

$$\frac{\partial^2 \mathbf{a}_\iota}{\partial \mathbf{u}_I \partial \vartheta_J} = \frac{\partial}{\partial \vartheta_J} \left(\frac{\partial \Lambda_2}{\partial \mathbf{u}_I} \Lambda_1 \mathbf{A}_\iota \right) = \frac{\partial \Lambda_2}{\partial \mathbf{u}_I} \frac{\partial \Lambda_1}{\partial \vartheta_J} \mathbf{A}_\iota, \quad (54b)$$

$$\begin{aligned} \frac{\partial^2 \gamma}{\partial \mathbf{u}_I \partial \vartheta_J} &= \frac{1}{2} \frac{\partial}{\partial \vartheta_J} \left(\frac{\partial \mathbf{a}_2}{\partial \mathbf{u}_I} \cdot \mathbf{a}_{3,1} + \mathbf{a}_2 \cdot \frac{\partial \mathbf{a}_{3,1}}{\partial \mathbf{u}_I} \right) \\ &= \frac{1}{2} \left(\frac{\partial \mathbf{a}_2}{\partial \mathbf{u}_I} \cdot \frac{\partial \mathbf{a}_{3,1}}{\partial \vartheta_J} + \frac{\partial^2 \mathbf{a}_2}{\partial \mathbf{u}_I \partial \vartheta_J} \cdot \mathbf{a}_{3,1} + \frac{\partial \mathbf{a}_2}{\partial \vartheta_J} \cdot \frac{\partial \mathbf{a}_{3,1}}{\partial \mathbf{u}_I} + \mathbf{a}_2 \cdot \frac{\partial^2 \mathbf{a}_{3,1}}{\partial \mathbf{u}_I \partial \vartheta_J} \right), \end{aligned} \quad (54c)$$

$$\begin{aligned} \frac{\partial^2 \mathbf{a}_{3,1}}{\partial \mathbf{u}_I \partial \vartheta_J} &= \frac{\partial}{\partial \vartheta_J} \left(\frac{\partial \Lambda_{2,1}}{\partial \mathbf{u}_I} \Lambda_1 \mathbf{A}_3 + \frac{\partial \Lambda_2}{\partial \mathbf{u}_I} \Lambda_{1,1} \mathbf{A}_3 + \frac{\partial \Lambda_2}{\partial \mathbf{u}_I} \Lambda_1 \mathbf{A}_{3,1} \right) \\ &= \frac{\partial \Lambda_{2,1}}{\partial \mathbf{u}_I} \frac{\partial \Lambda_1}{\partial \vartheta_J} \mathbf{A}_3 + \frac{\partial \Lambda_2}{\partial \mathbf{u}_I} \frac{\partial \Lambda_{1,1}}{\partial \vartheta_J} \mathbf{A}_3 + \frac{\partial \Lambda_2}{\partial \mathbf{u}_I} \frac{\partial \Lambda_1}{\partial \vartheta_J} \mathbf{A}_{3,1}. \end{aligned} \quad (54d)$$

Lastly, the second derivatives of the strains with respect to the nodal twist ϑ_I take the following

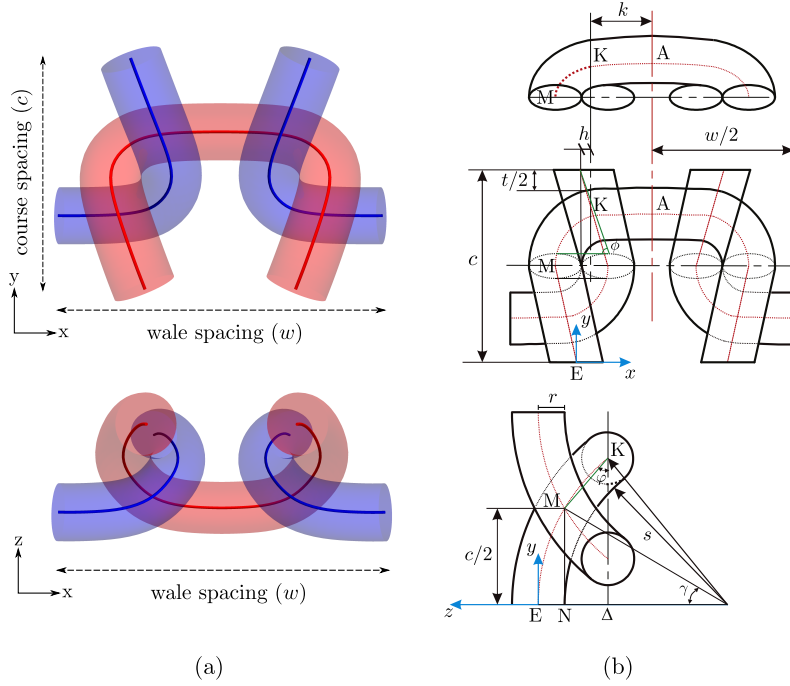


Figure 14. Geometry modelling of a weft-knitted RVE (a) Different views of a RVE of a weft-knitted textile (b) Introducing the geometric parameters that define the geometric description of the selected RVE [52].

forms.

$$\frac{\partial^2 \beta_l}{\partial \vartheta_I \partial \vartheta_J} = -\frac{\partial}{\partial \vartheta_J} \left(\frac{\partial \beta_l}{\partial \vartheta_I} \right) = -\frac{\partial}{\partial \vartheta_J} \left(\frac{\partial \mathbf{a}_l}{\partial \vartheta_I} \cdot \mathbf{a}_{1,1} \right) = -\frac{\partial^2 \mathbf{a}_l}{\partial \vartheta_I \partial \vartheta_J} \cdot \mathbf{a}_{1,1}, \quad (55a)$$

$$\frac{\partial^2 \mathbf{a}_l}{\partial \vartheta_I \partial \vartheta_J} = \frac{\partial}{\partial \vartheta_J} \left(\Lambda_2 \frac{\partial \Lambda_1}{\partial \vartheta_I} \mathbf{A}_l \right) = \Lambda_2 \frac{\partial^2 \Lambda_1}{\partial \vartheta_I \partial \vartheta_J} \mathbf{A}_l, \quad (55b)$$

$$\begin{aligned} \frac{\partial^2 \gamma}{\partial \vartheta_I \partial \vartheta_J} &= \frac{1}{2} \frac{\partial}{\partial \vartheta_J} \left(\frac{\partial \mathbf{a}_2}{\partial \vartheta_I} \cdot \mathbf{a}_{3,1} + \mathbf{a}_2 \cdot \frac{\partial \mathbf{a}_{3,1}}{\partial \vartheta_I} \right) \\ &= \frac{1}{2} \left(\frac{\partial \mathbf{a}_2}{\partial \vartheta_I} \cdot \frac{\partial \mathbf{a}_{3,1}}{\partial \vartheta_J} + \frac{\partial^2 \mathbf{a}_2}{\partial \vartheta_I \partial \vartheta_J} \cdot \mathbf{a}_{3,1} + \frac{\partial \mathbf{a}_2}{\partial \vartheta_J} \cdot \frac{\partial \mathbf{a}_{3,1}}{\partial \vartheta_I} + \mathbf{a}_2 \cdot \frac{\partial^2 \mathbf{a}_{3,1}}{\partial \vartheta_I \partial \vartheta_J} \right), \end{aligned} \quad (55c)$$

$$\begin{aligned} \frac{\partial^2 \mathbf{a}_{3,1}}{\partial \vartheta_I \partial \vartheta_J} &= \frac{\partial}{\partial \vartheta_J} \left(\Lambda_{2,1} \frac{\partial \Lambda_1}{\partial \vartheta_I} \mathbf{A}_3 + \Lambda_2 \frac{\partial \Lambda_{1,1}}{\partial \vartheta_I} \mathbf{A}_3 + \Lambda_2 \frac{\partial \Lambda_1}{\partial \vartheta_I} \mathbf{A}_{3,1} \right) \\ &= \Lambda_{2,1} \frac{\partial^2 \Lambda_1}{\partial \vartheta_I \partial \vartheta_J} \mathbf{A}_3 + \Lambda_2 \frac{\partial^2 \Lambda_{1,1}}{\partial \vartheta_I \partial \vartheta_J} \mathbf{A}_3 + \Lambda_2 \frac{\partial^2 \Lambda_1}{\partial \vartheta_I \partial \vartheta_J} \mathbf{A}_{3,1}. \end{aligned} \quad (55d)$$

B. GEOMETRY DEFINITION OF A WEFT-KNITTED RVE

The following equations for the geometry depicted in Figure 14 are extracted from Vassiliadis et al. [45] and smoothed at C^0 locations to recover the real smooth geometry of the RVE.

In part EM ($0 < y < c/2$):

$$x(y) = -\frac{2r}{c}y, \quad (56a)$$

$$z(y) = \sqrt{(s+r)^2 - y^2} - (s+r), \quad (56b)$$

where $s = \frac{1}{4r} \left[\left(c - r - \frac{t}{2} \right)^2 - \left(r + \frac{t}{2} \right)^2 \right]$.

In part MK ($c/2 < y < c/2 + R$):

$$x(y) = h - a \sqrt{1 - \left(\frac{y - c/2}{b} \right)^2}, \quad (57a)$$

$$z(y) = \sqrt{(s+r)^2 - y^2} - (s+r), \quad (57b)$$

where $h = \left(\frac{c}{2} - R \right) \tan \left(\frac{\pi}{2} - \phi \right)$, $R = \frac{c}{2} - \frac{t}{2} - r$, $\phi = \arctan \left(\frac{c - 2r \sin \gamma}{2r} \right)$ and $\gamma = \arcsin \left(\frac{c/2}{s+r} \right)$.

In part KA ($x(y = c/2 + R) < x < w/4$):

$$y(z) = \sqrt{(s+r)^2 - (z + s + r)^2}, \quad (58a)$$

$$z(x) = OZ - \sqrt{A^2 - (x - OX)^2}, \quad (58b)$$

where

$$OZ = [(x_2 - OX)^2 - (x_1 - OX)^2 + z_2^2 - z_1^2] / 2(z_2 - z_1),$$

$$A = \sqrt{(x_1 - OX)^2 + (z_1 - OZ)^2},$$

$$OX = w/4.$$

Additionally, (x_1, z_1) and (x_2, z_2) are the coordinates of two points in part MK with $y_1 = c/2 + R - 0.001$ and $y_2 = c/2 + R$.

A cubic B-spline curve was fitted at C^0 continuous locations namely, M and K. Moreover, this smooth curve EMKA is mirrored on the vertical axis passing at point A to obtain the complete geometry of the red yarn shown in Figure 14. Lastly, one smooth EMKA is rotated and translated appropriately to create the blue left yarn of Figure 14 and mirrored subsequently to complete the RVE geometry.

REFERENCES

1. J McCann, L Albaugh, V Narayanan, A Grow, W Matusik, J Mankoff, and J Hodgins. A compiler for 3D machine knitting. *ACM Transactions on Graphics*, 35:1–11, 2016.
2. M Popescu, M Rippmann, T Van Mele, and P Block. Automated generation of knit patterns for non-developable surfaces. In *Humanizing Digital Reality*, pages 271–284. Springer, 2018.
3. Y Luo, K Wu, T Palacios, and W Matusik. KnitUI: Fabricating interactive and sensing textiles with machine knitting. In *Proceedings of the 2021 CHI Conference on Human Factors in Computing Systems*, pages 1–12, 2021.
4. A Maziz, A Concas, A Khaldi, J Stålhand, N-K Persson, and E W H Jager. Knitting and weaving artificial muscles. *Science Advances*, 3:e1600327, 2017.
5. N-K Persson, J G Martinez, Y Zhong, A Maziz, and E W H Jager. Actuating textiles: next generation of smart textiles. *Advanced Materials Technologies*, 3:1700397, 2018.
6. K H Leong, S Ramakrishna, Z M Huang, and G A Bibo. The potential of knitting for engineering composites — a review. *Composites Part A: Applied Science and Manufacturing*, 31:197–220, 2000.
7. H Hasani, S Hassanzadeh, M J Abghary, and E Omrani. Biaxial weft-knitted fabrics as composite reinforcements: A review. *Journal of Industrial Textiles*, 46:1439–1473, 2017.
8. M Popescu, L Reiter, A Liew, T Van Mele, R J Flatt, and P Block. Building in concrete with an ultra-lightweight knitted stay-in-place formwork: prototype of a concrete shell bridge. In *Structures*, volume 14, pages 322–332, 2018.
9. D Perić, EA de Souza Neto, RA Feijóo, M Partovi, and AJ Carneiro Molina. On micro-to-macro transitions for multi-scale analysis of non-linear heterogeneous materials: unified variational basis and finite element implementation. *International Journal for Numerical Methods in Engineering*, 87:149–170, 2011.

10. M G D Geers, V G Kouznetsova, K Matouš, and J Yvonnet. Homogenization methods and multiscale modeling: Nonlinear problems. In *Encyclopedia of Computational Mechanics*. John Wiley & Sons, Ltd, 2017.
11. S Saeb, P Steinmann, and A Javili. Aspects of computational homogenization at finite deformations: a unifying review from reuss' to voigt's bound. *Applied Mechanics Reviews*, 68, 2016.
12. B Nadler, P Papadopoulos, and D J Steigmann. Multiscale constitutive modeling and numerical simulation of fabric material. *International Journal of Solids and Structures*, 43:206–221, 2006.
13. S Fillep, J Mergheim, and P Steinmann. Computational modelling and homogenization of technical textiles. *Engineering Structures*, 50:68–73, 2013.
14. D Liu, S Koric, and A Kontsos. A multiscale homogenization approach for architected knitted textiles. *Journal of Applied Mechanics*, 86:111006, 2019.
15. H Do, Y Y Tan, N Ramos, J Kiendl, and O Weeger. Nonlinear isogeometric multiscale simulation for design and fabrication of functionally graded knitted textiles. *Composites Part B: Engineering*, 202:108416, 2020.
16. M A Bessa, R Bostanabad, Z Liu, A Hu, D W Apley, C Brinson, W Chen, and W K Liu. A framework for data-driven analysis of materials under uncertainty: Countering the curse of dimensionality. *Computer Methods in Applied Mechanics and Engineering*, 320:633–667, 2017.
17. B A Le, J Yvonnet, and Q-C He. Computational homogenization of nonlinear elastic materials using neural networks. *International Journal for Numerical Methods in Engineering*, 104:1061–1084, 2015.
18. V Nguyen-Thanh, L Nguyen, T Rabczuk, and X Zhuang. A surrogate model for computational homogenization of elastostatics at finite strain using high-dimensional model representation-based neural network. *International Journal for Numerical Methods in Engineering*, 121:4811–4842, 2020.
19. L Wu, N G Kilingar, and L Noels. A recurrent neural network-accelerated multi-scale model for elastoplastic heterogeneous materials subjected to random cyclic and non-proportional loading paths. *Computer Methods in Applied Mechanics and Engineering*, 369:113234, 2020.
20. K Karapiperis, L Stainier, M Ortiz, and J E Andrade. Data-driven multiscale modeling in mechanics. *Journal of the Mechanics and Physics of Solids*, 147:104239, 2021.
21. A Platzer, A Leygue, L Stainier, and M Ortiz. Finite element solver for data-driven finite strain elasticity. *Computer Methods in Applied Mechanics and Engineering*, 379:113756, 2021.
22. C E Rasmussen and C K I Williams. *Gaussian processes for machine learning*. MIT Press, 2006.
23. J C Simo. A finite strain beam formulation. The three-dimensional dynamic problem. Part I. *Computer Methods in Applied Mechanics and Engineering*, 49:55–70, 1985.
24. J C Simo and L Vu-Quoc. A three-dimensional finite-strain rod model. part ii: Computational aspects. *Computer Methods in Applied Mechanics and Engineering*, 58:79–116, 1986.
25. A Cardona and M Geradin. A beam finite element non-linear theory with finite rotations. *International Journal for Numerical Methods in Engineering*, 26:2403–2438, 1988.
26. K Kondo, K Tanaka, and Atluri S N. An explicit expression for the tangent-stiffness of a finitely deformed 3-d beam and its use in the analysis of space frames. *Computers & Structures*, 24:253–271, 1986.
27. G Jelenić and M A Crisfield. Geometrically exact 3D beam theory: implementation of a strain-invariant finite element for statics and dynamics. *Computer methods in applied mechanics and engineering*, 171:141–171, 1999.
28. C Meier, A Popp, and W A Wall. An objective 3D large deformation finite element formulation for geometrically exact curved Kirchhoff rods. *Computer Methods in Applied Mechanics and Engineering*, 278:445–478, 2014.
29. A M Bauer, M Breitenberger, B Philipp, R Wüchner, and K-U Bletzinger. Nonlinear isogeometric spatial Bernoulli beam. *Computer Methods in Applied Mechanics and Engineering*, 303:101–127, 2016.
30. J C Simo, D D Fox, and M S Rifai. On a stress resultant geometrically exact shell model. Part II: The linear theory, computational aspects. *Computer Methods in Applied Mechanics and Engineering*, 73:53–92, 1989.
31. J C Simo and D D Fox. On a stress resultant geometrically exact shell model. Part I: Formulation and optimal parameterization. *Computer Methods in Applied Mechanics and Engineering*, 72:267–304, 1989.
32. F Cirak, M Ortiz, and P Schröder. Subdivision surfaces: A new paradigm for thin-shell finite-element analysis. *International Journal for Numerical Methods in Engineering*, 47:2039–2072, 2000.
33. F Cirak and M Ortiz. Fully c^1 -conforming subdivision elements for finite deformation thin-shell analysis. *International Journal for Numerical Methods in Engineering*, 51:813–833, 2001.
34. J Kiendl, K-U Bletzinger, J Linhard, and Wüchner R. Isogeometric shell analysis with Kirchhoff-Love elements. *Computer Methods in Applied Mechanics and Engineering*, 198:3902–3914, 2009.
35. F Cirak, Q Long, K Bhattacharya, and M Warner. Computational analysis of liquid crystalline elastomer membranes: Changing Gaussian curvature without stretch energy. *International Journal of Solids and Structures*, 51:144–153, 2014.
36. F Cirak and Q Long. Subdivision shells with exact boundary control and non-manifold geometry. *International Journal for Numerical Methods in Engineering*, 88:897–923, 2011.
37. Q Long, P B Bornemann, and F Cirak. Shear-flexible subdivision shells. *International Journal for Numerical Methods in Engineering*, 90:1549–1577, 2012.
38. M A Crisfield. *Non-linear finite element analysis of solids and structures*. John Wiley & Sons, 1997.
39. P G Ciarlet. *An Introduction to Differential Geometry with Applications to Elasticity*. Springer, 2006.
40. P Wriggers and G Zavarise. On contact between three-dimensional beams undergoing large deflections. *Communications in Numerical Methods in Engineering*, 13:429–438, 1997.
41. O Weeger, B Narayanan, L De Lorenzis, J Kiendl, and M L Dunn. An isogeometric collocation method for frictionless contact of Cosserat rods. *Computer Methods in Applied Mechanics and Engineering*, 321:361–382, 2017.

42. S Herath. *Multiscale modelling of woven and knitted fabric membranes*. PhD thesis, University of Cambridge, 2020.
43. T D Dinh, O Weeger, S Kaijima, and S K Yeung. Prediction of mechanical properties of knitted fabrics under tensile and shear loading: Mesoscale analysis using representative unit cells and its validation. *Composites Part B: Engineering*, 148:81–92, 2018.
44. O Weeger, A H Sakhaei, Y Y Tan, Y H Quek, T L Lee, S-K Yeung, S Kaijima, and M L Dunn. Nonlinear multi-scale modelling, simulation and validation of 3D knitted textiles. *Applied Composite Materials*, 25:1–14, 2018.
45. S Vassiliadis, A Kallivretaki, and C Provatidis. Geometrical modelling of plain weft knitted fabrics. *Indian Journal of Fibre and Textile Research*, 32:62–71, 2007.
46. P Wadekar, V Perumal, G Dion, A Kontsos, and D Breen. An optimized yarn-level geometric model for finite element analysis of weft-knitted fabrics. *Computer Aided Geometric Design*, 80:101883, 2020.
47. J Yvonnet, E Monteiro, and Q-C He. Computational homogenization method and reduced database model for hyperelastic heterogeneous structures. *International Journal for Multiscale Computational Engineering*, 11:201–225, 2013.
48. F Pedregosa, G Varoquaux, A Gramfort, V Michel, B Thirion, O Grisel, M Blondel, P Prettenhofer, R Weiss, V Dubourg, J Vanderplas, A Passos, D Cournapeau, M Brucher, M Perrot, and E Duchesnay. Scikit-learn: Machine learning in Python. *Journal of Machine Learning Research*, 12:2825–2830, 2011.
49. I M Sobol. Uniformly distributed sequences with an additional uniform property. *USSR Computational Mathematics and Mathematical Physics*, 16:236–242, 1976.
50. S Nezamabadi, J Yvonnet, H Zahrouni, and M Potier-Ferry. A multilevel computational strategy for handling microscopic and macroscopic instabilities. *Computer Methods in Applied Mechanics and Engineering*, 198:2099–2110, 2009.
51. C Miehe, J Schröder, and M Becker. Computational homogenization analysis in finite elasticity: material and structural instabilities on the micro-and macro-scales of periodic composites and their interaction. *Computer Methods in Applied Mechanics and Engineering*, 191:4971–5005, 2002.
52. S Vassiliadis, A Kallivretaki, and C Provatidis. Mechanical simulation of the plain weft knitted fabrics. *International Journal of Clothing Science and Technology*, 19:109–130, 2007.